



## TiN/(Al,Sc)N metal/dielectric superlattices and multilayers as hyperbolic metamaterials in the visible spectral range

Bivas Saha,<sup>1,2</sup> Gururaj V. Naik,<sup>2,3,\*</sup> Sammy Saber,<sup>1,2</sup> Cem Akatay,<sup>1,2</sup> Eric A. Stach,<sup>4</sup> Vladimir M. Shalaev,<sup>2,3</sup> Alexandra Boltasseva,<sup>2,3</sup> and Timothy D. Sands<sup>1,2,3,†</sup>

<sup>1</sup>*School of Materials Engineering, Purdue University, West Lafayette, Indiana 47907, USA*

<sup>2</sup>*Birck Nanotechnology Center, Purdue University, West Lafayette, Indiana 47907, USA*

<sup>3</sup>*School of Electrical and Computer Engineering, Purdue University, West Lafayette, Indiana 47907, USA*

<sup>4</sup>*Center for Functional Nanomaterials, Brookhaven National Laboratory, Upton, New York 11973-5000, USA*

(Received 14 June 2014; revised manuscript received 22 August 2014; published 12 September 2014)

Hyperbolic metamaterials (HMMs) based on metal/dielectric multilayers have garnered attention in recent years due to their extraordinary optical properties emanating from hyperbolic dispersion of isofrequency surfaces. We have developed a new class of epitaxial metal/dielectric superlattice HMMs based on transition-metal nitrides—titanium nitride (TiN) and aluminum scandium nitride ( $\text{Al}_x\text{Sc}_{1-x}\text{N}$ )—that could potentially lead to better HMM performance without requiring any traditional plasmonic materials such as gold (Au) and silver (Ag). Our results suggest that the TiN/(Al,Sc)N superlattices grown on (001) MgO substrates are nominally monocrystalline and pseudomorphic, exhibiting sharp interfaces with interface roughnesses of about one to two atomic layers. HMMs deposited on (0001) sapphire substrates grow in 111 orientation with local epitaxy inherent to individual grains, while on (001) Si substrates, the HMMs are polycrystalline. The HMM properties extracted with effective medium theory along with nonlocal field corrections indicate that the TiN/(Al,Sc)N superlattices grown on MgO substrates have both transverse negative (type-I) and transverse positive (type-II) hyperbolic dispersion of the isofrequency surfaces in the visible to near-IR spectral regions. The carrier concentration of TiN layers was varied deliberately by tuning the deposition conditions, thereby shifting the spectral range of both type-I and type-II HMM dispersions. The epitaxial thin-film-based HMMs developed here mark the beginning of a new generation of optical metamaterials with enhanced electromagnetic properties.

DOI: [10.1103/PhysRevB.90.125420](https://doi.org/10.1103/PhysRevB.90.125420)

PACS number(s): 68.65.Cd, 78.20.-e, 78.67.Pt

### I. INTRODUCTION

Hyperbolic metamaterials [1,2] (HMMs) are promising candidates for achieving subnanometer-resolution imaging [3,4], subwavelength light concentration [5], negative refraction [6,7], and engineered absorption and emission from quantum emitters [8–10]. Hyperbolic dispersion in metal/dielectric superlattices gives rise to extremely high photonic densities of states over a broad spectral range that may be useful in next-generation optoelectronic devices such as single-photon guns [2], efficient heat sinks [11], and thermophotovoltaics [12]. The usefulness of the metal/dielectric superlattice-based HMM systems for the above applications, however, critically depends on the constituent materials. The nanoscale superlattices must have superior crystal quality and sharp superlattice interfaces to minimize losses that are detrimental to device performance.

Conventional metal/dielectric superlattices for HMM application in the visible and near-infrared ranges use noble metals [13] such as gold and silver as their metallic components. Noble metals, however, have large magnitudes of the real and imaginary permittivity, and are therefore not well suited for practical HMM applications. Additionally, growing ultrathin, smooth and continuous layers of noble metals in a superlattice

is extremely difficult owing to their large surface energies. Noble metals also have low melting temperatures, limiting the possibility of HMMs for high-temperature applications.

On the contrary, alternative plasmonic materials [14] such as titanium nitride (TiN) can be grown in a superlattice with epitaxial quality. In contrast to noble metals, TiN has a low surface energy ( $63 \text{ mJ/m}^2$ ), is mechanically hard (24 GPa), stable at high temperatures (melting point  $2700^\circ\text{C}$ ), complementary metal-oxide semiconductor (CMOS) compatible, and has moderate negative real permittivity in the visible spectral range. All these properties make TiN a well-suited plasmonic material for superlattice HMM applications.

Yet, to grow high-quality epitaxial superlattices with TiN as a plasmonic component, we must also have a dielectric that has the same crystal structure (rocksalt) and lattice constant ( $4.24 \text{ \AA}$ ) as TiN, and the dielectric should also possess low surface energy and compatible dielectric permittivities with TiN to achieve the desired HMM properties. We have developed aluminum scandium nitride ( $\text{Al}_x\text{Sc}_{1-x}\text{N}$ ) as a rocksalt dielectric with tunable structural and optical properties that are compatible with TiN. A detailed discussion of the growth and characterization as well as the optical and electronic properties of rocksalt- $\text{Al}_x\text{Sc}_{1-x}\text{N}$  is presented in Ref. [15]. In the present paper, we present a comprehensive analysis of TiN/(Al,Sc)N superlattice growth and characterization, and connect the structural properties of the HMMs with their optical characteristics. The superlattice samples are grown with dc-magnetron sputtering technique inside a high vacuum chamber. Details about the growth and characterization methods are presented in Ref. [15].

\*Present address: Department of Materials Science and Engineering, Stanford University, 496 Lomita Mall, Stanford, California 94305-4034, USA.

†Present address: Office of the President, Burruss Hall, Suite 210, 800 Drillfield Drive, Blacksburg, VA, 24061.

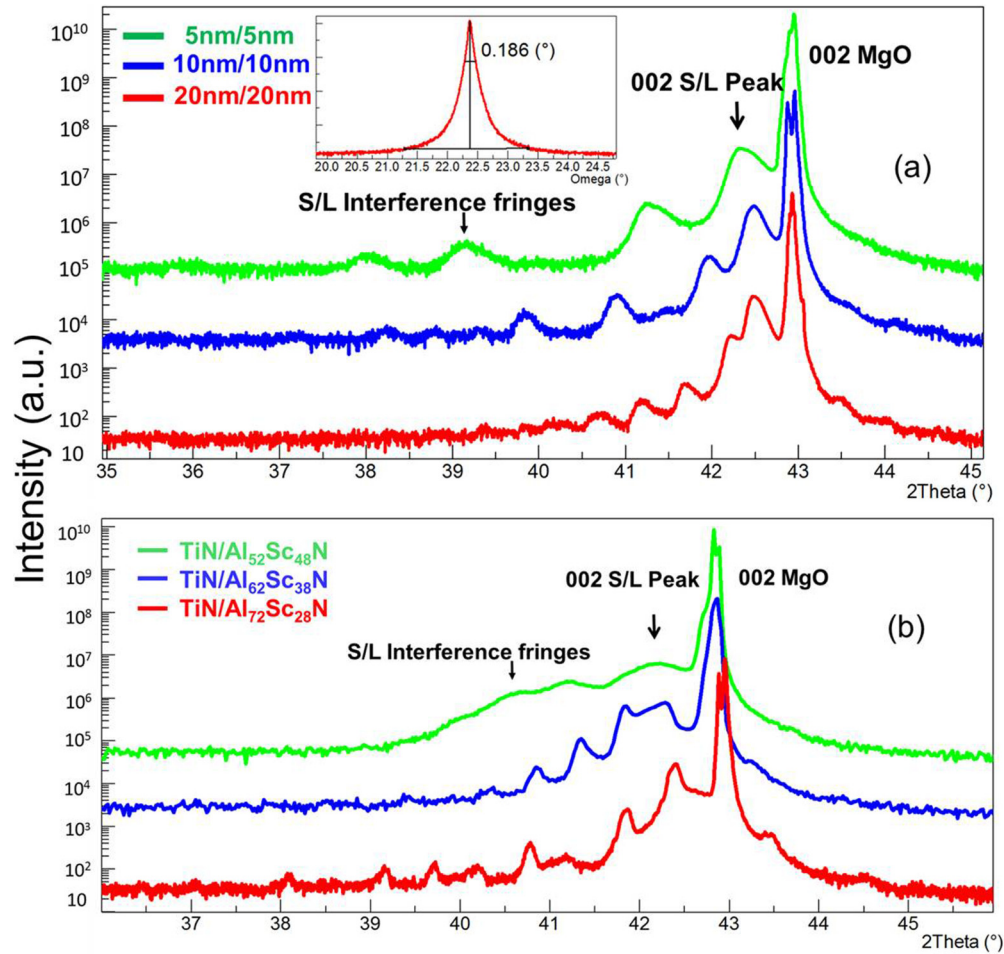


FIG. 1. (Color online) (a) Symmetric  $2\theta$ - $\omega$  x-ray diffraction spectra of TiN/Al<sub>0.72</sub>Sc<sub>0.28</sub>N superlattices grown on (002) MgO substrates are presented as a function of the superlattice periodicity. The spectra suggest that all the superlattices grow with (002) orientations with sharp interference fringes. The inset in the figure shows that the FWHM of the rocking curve is extremely small due to the single crystal epitaxial superlattice growth. (b) X-ray diffraction spectra of the superlattices on MgO substrates where the AlN mole fraction in the Al<sub>x</sub>Sc<sub>1-x</sub>N is varied. For the TiN/Al<sub>0.72</sub>Sc<sub>0.28</sub>N, TiN/Al<sub>0.62</sub>Sc<sub>0.38</sub>N superlattice, the interference fringes are clearly visible; however, for the TiN/Al<sub>0.52</sub>Sc<sub>0.48</sub>N superlattice interference fringes are diffused suggesting rough interface.

## II. GROWTH AND STRUCTURAL CHARACTERIZATION

### A. X-ray diffraction of superlattices grown on MgO substrates

Crystal quality and crystal orientations of the superlattices were investigated by high-resolution x-ray diffraction employing both symmetric and asymmetric scans, reciprocal space x-ray maps, and x-ray reflectivity. The symmetric  $2\theta$ - $\omega$  x-ray diffraction spectra [see Fig. 1(a)] of  $m/n$  TiN/Al<sub>0.72</sub>Sc<sub>0.28</sub>N superlattices [where  $m$  and  $n$  represent the thicknesses in nanometers of TiN and (Al,Sc)N layers, respectively] grown on (001) MgO substrates indicate that the superlattices grow with (002) crystal orientation. The (002) diffraction peaks of the 20 nm/20 nm, 10 nm/10 nm, and 5 nm/5 nm superlattices grown at 850 °C are located at 42.50°, 42.49°, and 42.33°, respectively, representing out-of-plane lattice constants ( $c$ ) of 4.25, 4.25, and 4.27 Å. From our previous analysis [15], we know that the TiN and rocksalt Al<sub>0.72</sub>Sc<sub>0.28</sub>N thin films have out-of-plane lattice constants of 4.24 and 4.29 Å, respectively. Hence, the measured  $c$ -axis lattice constant represents an averaged out-of-plane lattice constant of the individual layers.

Interference fringes are clearly visible in all of the diffraction spectra, which suggest sharp and abrupt superlattice interfaces with very small roughness and intermixing. The full width at half maximum (FWHM) of the rocking curves ( $\omega$  scan) are 0.15°, 0.18°, and 0.43° for the three superlattices having period thicknesses of 40, 20, and 10 nm, respectively. The small values of the FWHM of the rocking curve indicate that the superlattices are nominally monocrystalline with a small degree of mosaicity when grown on (001) MgO substrates. Since MgO has a lattice constant of 4.21 Å, pseudomorphic superlattices experience biaxial compressive strain, which reduces the in-plane lattice constant ( $a$ ) while slightly increasing the out-of-plane lattice constant ( $c$ ).

For the 10 nm/10 nm TiN/Al<sub>0.72</sub>Sc<sub>0.28</sub>N superlattices grown at 650 °C, 750 °C, and 850 °C, the out-of-plane lattice constants ( $c$ ) are 4.27, 4.26, and 4.25 Å, respectively. This suggests that the strain relaxation is more pronounced at higher growth temperatures. However, the FWHM of the rocking curve increases from 0.05° for the superlattice grown at 650 °C, to 0.07° and 0.19°, respectively, for the superlattices deposited

TABLE I. Out-of-plane ( $c$ ) and in-plane ( $a$ ) lattice constants of  $\text{Al}_x\text{Sc}_{1-x}\text{N}$  as a function of  $x$  (adapted from our previous work to explain the results of Ref. [15]).

$x$ in $\text{Al}_x\text{Sc}_{1-x}\text{N}$ layers	Out-of-plane lattice constant ( $c$ ) Å	In-plane lattice constant ( $a$ ) Å
0.52	4.37	4.29
0.62	4.31	4.25
0.72	4.29	4.22

at 750 °C and 850 °C. The increasing trend in the FWHM of the rocking curve with temperature suggests that with higher growth temperatures the degree of mosaicity increases. This observation is consistent with the local strain inhomogeneity associated with misfit dislocations in relaxed films grown at higher temperatures.

We have also varied the interface roughness of the superlattices deliberately by changing the mole fraction of aluminum nitride (AlN) ( $x$ ) in  $\text{Al}_x\text{Sc}_{1-x}\text{N}$  layers, which, in turn, changes its lattice constant. As mentioned in Table I, both the out-of-plane and in-plane lattice constants of  $\text{Al}_x\text{Sc}_{1-x}\text{N}$  decrease with the increase in  $x$ . Note that the difference in the (002) peak position for the  $x$ -ray diffraction spectra of the  $\text{TiN}/\text{Al}_{0.52}\text{Sc}_{0.48}\text{N}$ ,  $\text{TiN}/\text{Al}_{0.62}\text{Sc}_{0.38}\text{N}$ , and  $\text{TiN}/\text{Al}_{0.72}\text{Sc}_{0.28}\text{N}$  superlattices [Fig. 1(b)] grown at 750 °C is very small. This is because the  $\text{Al}_x\text{Sc}_{1-x}\text{N}$  layers in all superlattices are strained and acquire lattice constant values close to that of TiN. The total thickness of each of these superlattices is 200 nm and strain does not fully relax over this thickness range. There is, however, one noticeable difference: Whereas the interference fringes are very sharp and pronounced for the superlattices with  $x = 0.62$  and 0.72, suggestive of sharp and smooth interfaces, for the  $\text{TiN}/\text{Al}_{0.52}\text{Sc}_{0.48}\text{N}$  superlattice, the interference fringes are much more diffuse and weak, indicative of interface roughness and possibly intermixing across the interfaces.

### B. Reciprocal space x-ray map

A reciprocal space x-ray diffraction map on a 10 nm/10 nm  $\text{TiN}/\text{Al}_{0.72}\text{Sc}_{0.28}\text{N}$  superlattice (Fig. 2) demonstrates that the superlattices are pseudomorphic and epitaxial with the MgO(001) substrates. Figure 2 indicates the (024) MgO and the (024) superlattice diffraction peaks along with two interference fringes, which are aligned vertically having the same  $Q_x$  values. This suggests that along the in-plane directions the lattice constants of TiN, and  $\text{Al}_{0.72}\text{Sc}_{0.28}\text{N}$  layers are fixed to that of MgO (4.21 Å). Along the cross-plane directions, however, the lattice constant of the superlattice is measured to be 4.26 Å. The two interference fringes are equally spaced from the middle (024) superlattice peak corresponding to the periodicity of the superlattice.

### C. X-ray reflectivity

X-ray reflectivity (XRR) studies [16] have been employed to understand the interface roughness and intermixing of atoms at the interfaces of the superlattices. XRR studies have also been used to accurately determine the individual layer

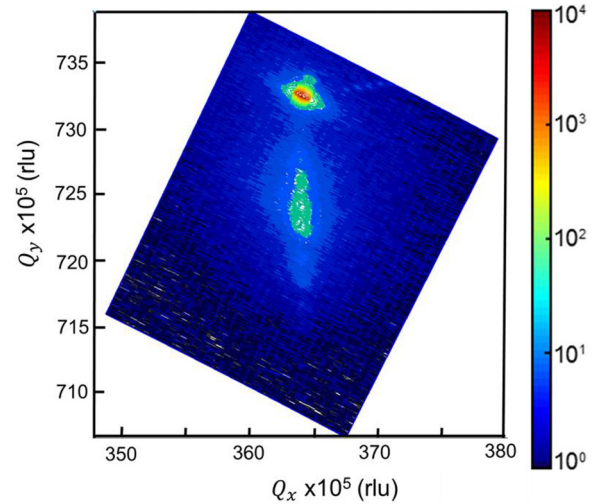


FIG. 2. (Color online) Reciprocal space x-ray map of a  $\text{TiN}/\text{Al}_{0.72}\text{Sc}_{0.28}\text{N}$  superlattice. The (024) MgO and the superlattice peak are aligned vertically which suggest that the superlattices are pseudomorphic.

thicknesses and periodicity of the superlattices. The specular XRR spectrum of a 10 nm/10 nm  $\text{TiN}/\text{Al}_{0.72}\text{Sc}_{0.28}\text{N}$  eight-period superlattice [see Fig. 3(a)] shows sharp periodic x-ray reflection fringes known as Kiessig fringes that arise due to x-ray reflection at different interfaces. The intensities of these fringe peaks are related to the sharpness of the interfaces. As the total superlattice thickness ( $\sim 200$  nm) is much larger than the individual period thickness ( $\sim 20$  nm), there are also background Kiessig fringes closely spaced together that represent the total thickness of the superlattice. We have fitted these data and corroborated the surface roughness derived from the data fitting with that of the surface roughness measured by atomic force microscopy. The interface roughness as a function of the superlattice periodicity [Fig. 3(c)] suggests that the first TiN layer that grows on the (001) MgO substrate has a roughness of  $\sim 0.36$  nm (rms). Since the lattice mismatch between TiN and MgO is less than 1%, the interface is coherent and lattice planes are matched resulting in a small value of roughness. For all other TiN layers that are grown on  $\text{Al}_{0.72}\text{Sc}_{0.28}\text{N}$  layers, the interface roughness is still very small at  $\sim 0.35$ – $0.5$  nm, corresponding to about two atomic layers. The roughness increases as a function of the superlattice periodicity primarily due to an increasing degree of strain relaxation. Although TiN and  $\text{Al}_{0.72}\text{Sc}_{0.28}\text{N}$  are closely lattice matched, they are not perfectly matched, and this results in some residual strain buildup during growth. Eventually, the stored strain energy is released through plastic deformation or roughening as the total thickness increases. The  $\text{Al}_{0.72}\text{Sc}_{0.28}\text{N}$  layers grown on top of TiN layers, however, have interface roughnesses in the range of 0.15–0.30 nm, i.e., about one monolayer. Like the TiN case, the interface roughness also increases with an increase in superlattice periodicity due to strain relaxation. The small value of interface roughness measured here is an indication of the atomically sharp interfaces that are critical for not just optical metamaterial applications, but also for several other optical and optoelectronic devices. We must also note that the lattice-matched  $\text{TiN}/(\text{Al,Sc})\text{N}$  superlattice crystal quality

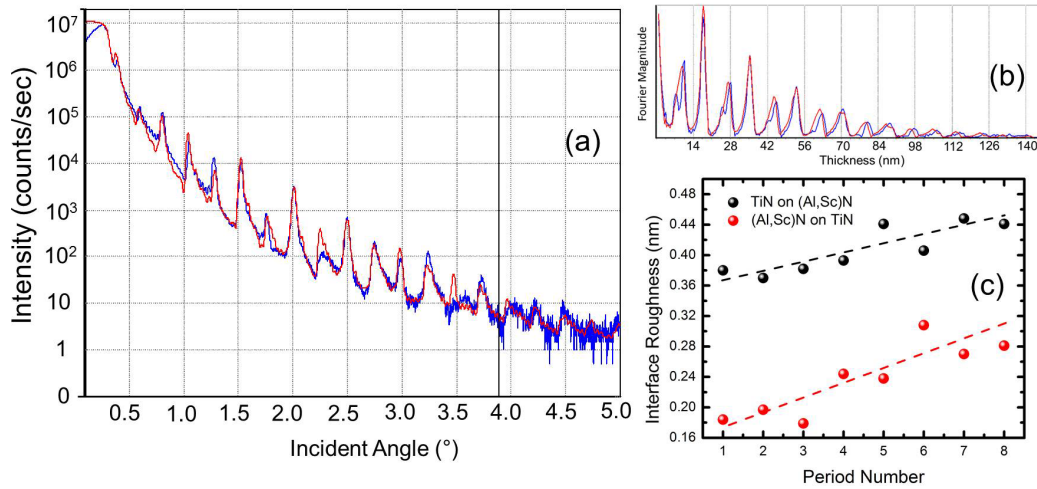


FIG. 3. (Color online) (a) XRR spectra of a 10 nm/10 nm eight-period TiN/Al<sub>0.72</sub>Sc<sub>0.28</sub>N superlattice along with the simulated data. Sharp and clear Kiessig fringes are clearly visible that arise due to x-ray reflection from the superlattice interfaces. Careful observations of the spectrum also show fringes that represent the total thickness of the superlattice. (b) Fourier transform magnitude as a function of the thickness shows two different types of peaks: one that arises from total period thickness and the other closely spaced doublet that arises from the thickness of the individual layers. (c) Extracted interface roughnesses are presented as a function of the superlattice periodicity which suggests that the interface roughness is of the order of one to two atomic layers.

and interface properties resemble the well-studied arsenide [17] semiconductor device heterostructure systems such as GaAs/AlAs, InGaAs/InAlAs.

The difference in the interface roughness between TiN/Al<sub>0.72</sub>Sc<sub>0.28</sub>N and Al<sub>0.72</sub>Sc<sub>0.28</sub>N/TiN may be related to a difference in the surface energies of the constituent materials. Although TiN has a lower surface energy [18] (~ 63 mJ/m<sup>2</sup>) compared to most elemental metals, (Al,Sc)N is likely to have an even lower surface energy and sharper cusps in the Wulff plot, as it is a semiconductor with saturated bonds and high ionicity. Under these conditions, the free (Al,Sc)N surface would be expected to be faceted to a greater degree than the free TiN surface.

#### D. X-ray diffraction of superlattices grown on sapphire and Si substrates

X-ray diffraction of the superlattices grown on (0001) sapphire substrates is presented in Fig. 4. The symmetric

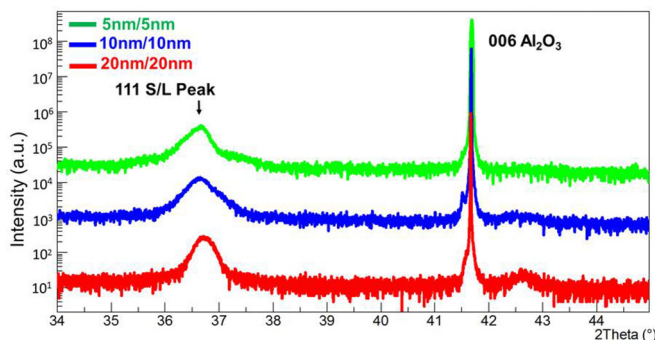


FIG. 4. (Color online) X-ray diffraction spectra of superlattices grown on (0001) sapphire substrate. Superlattices grow with (111) orientations on sapphire substrates with not so sharp interference fringes which indicate that the interfaces are not atomically smooth.

$2\theta$ - $\omega$  diffraction spectra suggest that the superlattices grow with (111) orientation with the (111) peak located at  $\sim 36.6^\circ$ . The sapphire (006) diffraction peak can also be seen in the spectra. The interference fringes are not pronounced, which indicates that the interfaces are rougher than the superlattices grown on MgO substrates. The (111) peak position does not change appreciably with the change in superlattice periodicity for samples grown at the same temperature. The out-of-plane lattice constant ( $c$ ) of the 20 nm/20 nm, 10 nm/10 nm, and 5 nm/5 nm superlattices grown at 650 °C are calculated to be 4.23, 4.24, and 4.24 Å, respectively, which are consistent with the lattice parameters of samples grown on MgO substrates. In the x-ray diffraction (XRD) spectrum, a wurtzite Al<sub>0.72</sub>Sc<sub>0.28</sub>N peak is not present, which suggests that inside the superlattice, the rocksalt (cubic) Al<sub>0.72</sub>Sc<sub>0.28</sub>N phase is epitaxially stabilized. Although the interface quality of the superlattices grown on (0001) sapphire is not as good as those on MgO, these superlattices are still have a local epitaxy inherent to the grains. The asymmetric phi scan (not presented here) indicates six main peaks that are 60° apart, suggesting that the superlattices grow with two main variants.

We have grown TiN/(Al,Sc)N superlattices on (001) Si substrates as well. The superlattices grow as polycrystalline films on Si substrates. Thus, no appreciable XRD signal from these polycrystalline superlattices is observed as the total thickness is too small (~200 nm).

#### E. TEM and dark field scanning tunneling electron microscopy analysis

The microstructure and the interface quality of the superlattices have been evaluated by high-resolution transmission electron microscopy (HRTEM) and medium-angle annular dark field scanning transmission electron microscopy (MAADF-STEM). The superlattice sample used for the TEM analysis had a TiN layer thickness fixed at 20 nm, while the Al<sub>0.72</sub>Sc<sub>0.28</sub>N layer thickness was increased from 2 to 80 nm in steps of

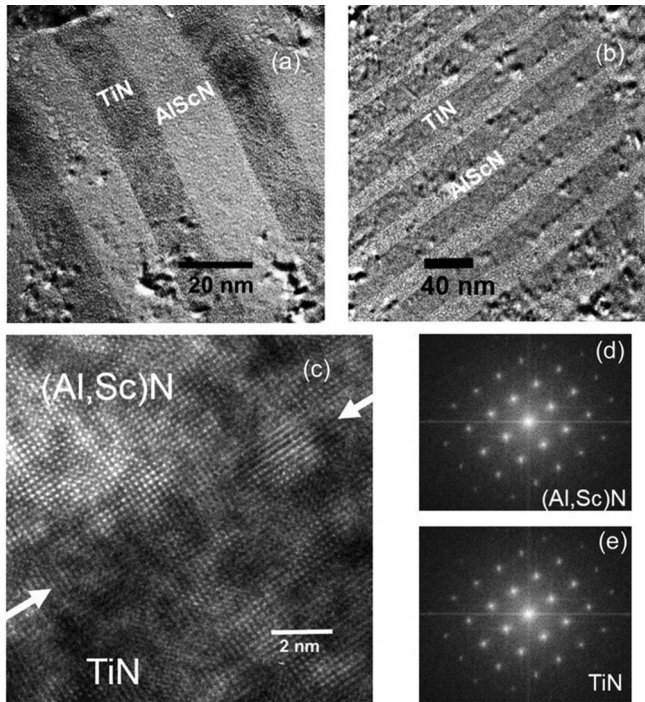


FIG. 5. (a), (b) HRTEM image of TiN/ $\text{Al}_{0.72}\text{Sc}_{0.28}\text{N}$  superlattices grown on (001) MgO substrate. The TiN and  $\text{Al}_{0.72}\text{Sc}_{0.28}\text{N}$  layers are separated by sharp and abrupt interfaces. (c) High-magnification image of a TiN/ $\text{Al}_{0.72}\text{Sc}_{0.28}\text{N}$  interface that shows cube-on-cube epitaxial crystal growth. Fourier transform diffraction patterns suggest that both the TiN and  $\text{Al}_{0.72}\text{Sc}_{0.28}\text{N}$  layers have rocksalt crystal structure.

2 nm until the  $\text{Al}_{0.72}\text{Sc}_{0.28}\text{N}$  layer thickness reached 20 nm, and in steps of 4 nm thereafter. The TEM image in Fig. 5(a) shows a clear and distinct interface between the (001) MgO and (001) TiN layers. The closely matched lattice constant (mismatch less than 1%) of TiN and the MgO substrate ensures that the growth of the initial layers is smooth. Both TiN and  $\text{Al}_{0.72}\text{Sc}_{0.28}\text{N}$  layers are uniform in thickness and have distinctly sharp superlattice interfaces [Fig. 5(b)]. Even the 4 nm  $\text{Al}_{0.72}\text{Sc}_{0.28}\text{N}$  layer is clearly visible, suggesting that there is not much intermixing at the interface, consistent with the XRR analysis. The high-magnification image of the TiN/ $\text{Al}_{0.72}\text{Sc}_{0.28}\text{N}$  interface [Fig. 5(c)] shows the cube-on-cube epitaxial relationship of  $\text{TiN}(001)[100]||\text{MgO}(001)[100]$  and  $\text{Al}_{0.72}\text{Sc}_{0.28}\text{N}(001)[100]||\text{TiN}(001)[100]$ . The interfaces are coherent, lattice matched, and pseudomorphic. No signatures of misfit dislocations at the interfaces were observed in our microscopy images. A fast Fourier transformation of the image from an  $\text{Al}_{0.72}\text{Sc}_{0.28}\text{N}$  region [Fig. 5(c)] indicates a rocksalt (cubic) diffraction pattern, which is consistent with metastable rocksalt (cubic)  $\text{Al}_{0.72}\text{Sc}_{0.28}\text{N}$  layers between TiN layers. The TEM micrograph of a superlattice sample grown on a (001) Si substrate [Fig. 6(a)] indicates polycrystalline superlattice growth as expected. The interfaces are much rougher and atomically diffused. Dark field TEM images [Fig. 6(b)] clearly show the presence of grain boundaries.

While the conventional HRTEM analysis provides a microstructural overview of the superlattices by resolving the structure at the atomic level, we have also employed elemental

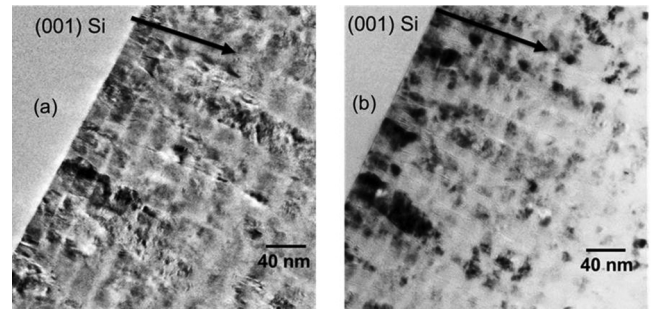


FIG. 6. (a) HRTEM image of TiN/ $\text{Al}_{0.72}\text{Sc}_{0.28}\text{N}$  superlattice grown on (001) Si substrate. The superlattice is polycrystalline on Si substrates with rough and atomically diffused interfaces. (b) Dark field HRTEM image of the superlattice that shows grain boundaries of the polycrystalline sample.

analysis of the interface via STEM-EELS (electron-energy-loss spectroscopy) in MAADF-STEM [19] mode. The TiN layers appear bright and uniform, whereas the  $\text{Al}_{0.72}\text{Sc}_{0.28}\text{N}$  layers appear dark due to the higher atomic number of Ti compared to Al. As in the case of normal TEM images, even a 2-nm-thick  $\text{Al}_{0.72}\text{Sc}_{0.28}\text{N}$  layer is clearly distinguishable.

The chemical nature of the layers is further confirmed by EELS analysis on the individual superlattice layers [Fig. 7(b)]. The EELS nitrogen  $K$  edge and scandium  $L_{2,3}$  edge are positioned at  $E_{\text{N}} = 401$  eV and  $E_{\text{Sc}} = 402$  eV, respectively (not shown here). Due to overlap of these edges, nitrogen and scandium cannot be distinguished and the plotted EELS signal will have contributions from both elements. Titanium, on the other hand, has a sharp  $L_{2,3}$  edge at  $E_{\text{Ti}} = 456$  eV and is clearly distinguished (not shown here). The EELS line scan was performed along the line in the region shown in Fig. 7(c). The EELS signals for Sc + N and Ti are plotted as a function of position on the line. The Ti signal originates from the TiN layer and exhibits a layer thickness of 18–20 nm for the three layers scanned. In the regions where the Ti signal is negligible, the Sc + N signal increases due to the presence of the  $\text{Al}_{0.72}\text{Sc}_{0.28}\text{N}$  layer. The EELS profile confirms the alternating layer structure.

Careful observation of the images revealed [Fig. 7(a)] that there are structural V-shaped defects in the superlattices. These defects are located on the (120) planes and originate from the initial growth layer at the MgO interface suggesting that the interfaces are the nucleation points. Since the crystal structure of MgO is also rocksalt, there are two possibilities that could give rise to such defects: (1) there is a specific crystallographic defect (other than a simple step edge) on the MgO surface that may be related to a second phase or perhaps a stacking fault. TiN nucleates on that defect with a displacement vector component along the surface normal that is not coincident with a lattice vector. The result is that the growth front on top of the defect leads the growth front of surrounding material, providing an opportunity for lateral growth that creates a “V” defect. It appears that the defect is such that the interface could be voided at the atomic level. (2) The small degree of lattice mismatch between TiN and MgO is sufficient to nucleate an extended defect at the interface that has an effective Burgers vector component in the plane of the interface (as well as out of plane).

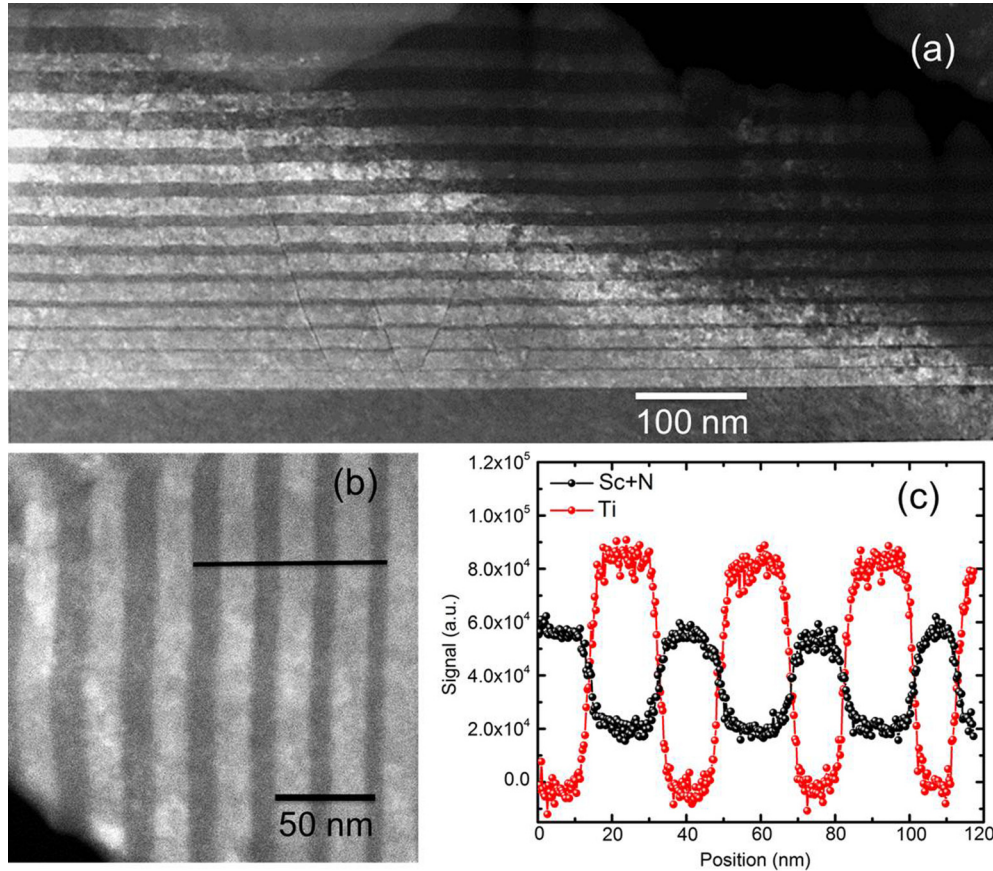


FIG. 7. (Color online) (a) MAADF-STEM image of the superlattice. TiN layers appear bright in the spectra because of higher atomic number of Ti atoms, while the  $\text{Al}_{0.72}\text{Sc}_{0.28}\text{N}$  layers look dark. Even the 2 nm  $\text{Al}_{0.72}\text{Sc}_{0.28}\text{N}$  layer is clearly visible in the STEM image. The “V”-shaped structural defects are observed in the dark field STEM image, which are seen to be originating from the MgO substrate. (b) A high-magnification MAADF-STEM image of the superlattice showing sharp superlattice interface and uniform individual layer thickness. (c) EELS line scan across the interface corresponding to figure (b) that shows sharp and abrupt Ti edges in the TiN layer. As scandium and nitrogen signals are plotted together the interface edges are a little diffused. It is also seen from the image that the TiN layer thickness is approximately constant at 18–20 nm, while the  $\text{Al}_{0.72}\text{Sc}_{0.28}\text{N}$  layer thickness is decreasing from left to right.

The MAADF-STEM analysis on the superlattice grown on the (001) Si substrate indicates that the interfaces are wavy and rough (Fig. 8). Grain boundaries are also clearly visible

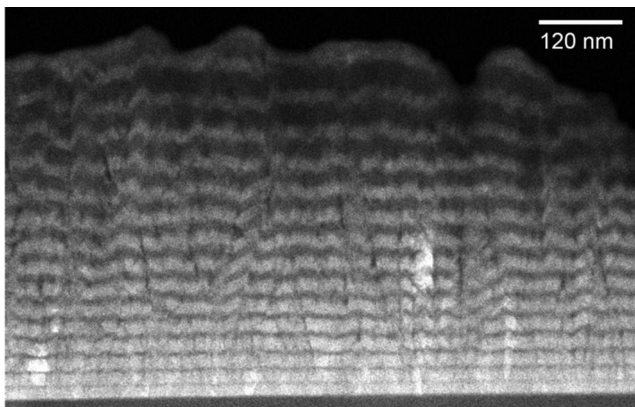


FIG. 8. An MAADF-STEM image of superlattice grown on (001) Si substrate. It is clear from the image that the interfaces are atomically diffused and rough. The superlattice is polycrystalline on Si substrate, and the grain boundaries are clearly visible.

in the images. Although the roughness of the interfaces in this case is much greater than in the superlattices grown on MgO substrates, thin  $\text{Al}_{0.72}\text{Sc}_{0.28}\text{N}$  layers are still visible in the images.

### III. OPTICAL PROPERTIES OF TiN/(Al,Sc)N SUPERLATTICE METAMATERIALS

In this section, the connection between the structural aspects and optical HMM properties is discussed. In order to enable HMM applications in practical optical devices, one needs low loss, high figure-of-merit [14] superlattices that are free from structural defects, stable at high temperatures, and ideally, CMOS compatible. Before discussing HMM properties, we describe the optical properties of TiN and (Al,Sc)N thin films having a thickness of 80–100 nm.

#### A. Dielectric properties

TiN has generated considerable interest in the research community as its optical properties resemble those of gold in the visible spectral range [20], albeit with slightly higher optical losses. TiN shows its metallic or plasmonic character

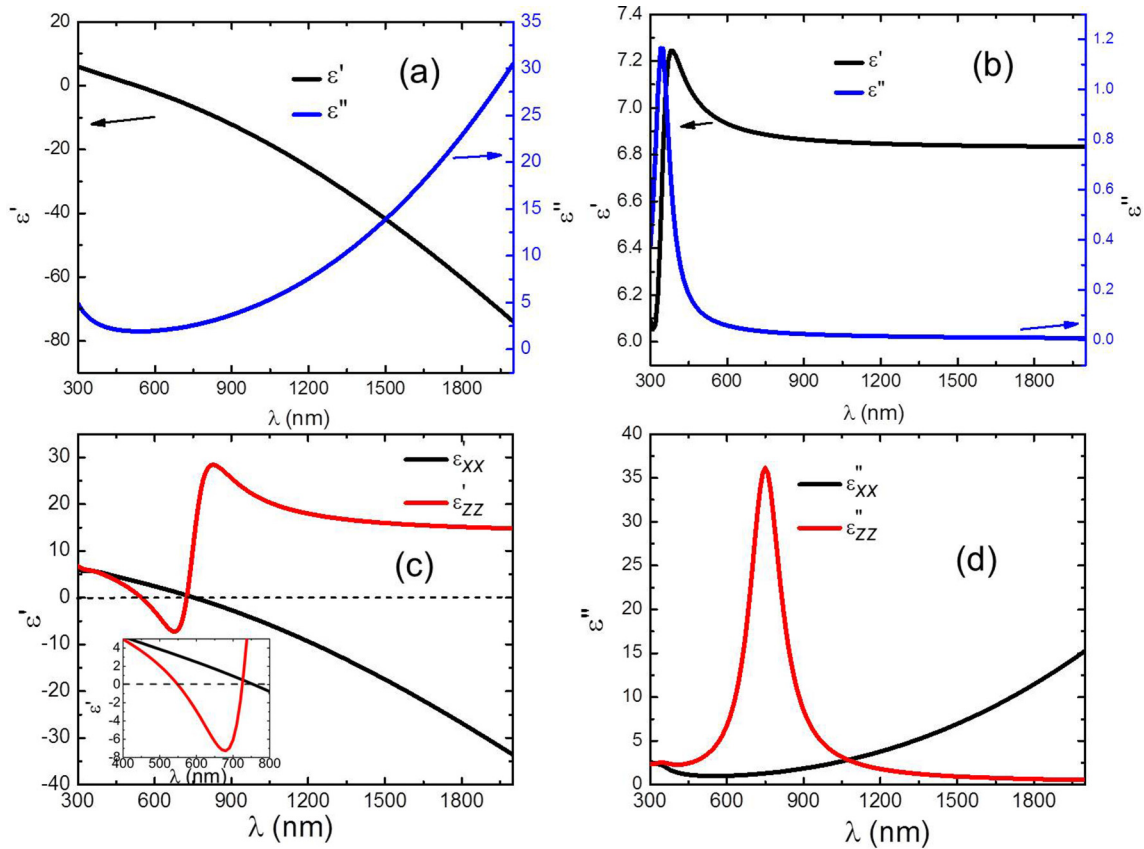


FIG. 9. (Color online) (a) The real ( $\epsilon'$ ) and imaginary ( $\epsilon''$ ) parts of the dielectric permittivity of TiN layers show that TiN becomes metallic in the green part of the spectrum at the 480–500 nm spectral range. The optical loss is slightly high in the visible spectral range due to interband transitions. (b) Dielectric permittivity of the  $\text{Al}_{0.72}\text{Sc}_{0.28}\text{N}$  layers suggests that  $\epsilon'$  has a peak at  $\sim 430$  nm spectral range due to interband transition, but is roughly constant at 6.8 from the 500–2000 nm spectral region. The optical loss expressed by  $\epsilon''$  is extremely small in the visible to near-IR range. (c) The anisotropic dielectric permittivity of the TiN/ $\text{Al}_{0.72}\text{Sc}_{0.28}\text{N}$  superlattices is presented calculated by the EMT. The plot shows that before the 480 nm spectral range when TiN behaves as a dielectric material, both  $\epsilon'_{xx}$  and  $\epsilon'_{zz}$  are positive. Above the 480 nm but below the 720 nm spectral range,  $\epsilon'_{xx}$  is positive but  $\epsilon'_{zz}$  is negative, which gives rise to type-I HMM dispersion. The sign of the permittivity reverses in the higher wavelength regions to give type-II dispersion. (d)  $\epsilon''_{xx}$  remains very small in the visible spectral range and only increases in the IR regime due to the free carrier Drude absorption, while the  $\epsilon''_{zz}$  has a peak at  $\sim 750$  nm as the metamaterial undergoes a type-I to type-II dispersion of its isofrequency surface.

starting from the green part of the visible spectrum ( $\sim 480$ –500 nm) to longer wavelengths. The magnitude of  $\epsilon'$  of TiN increases rather slowly with increasing wavelength compared to gold. But unlike gold, TiN is a refractory transition-metal nitride [21] that can be doped or alloyed and can be grown as ultrathin films, offering the flexibility required for the realization of practical devices. The only significant drawback of TiN is the optical loss arising due to interband transitions in the visible spectral range. Recent reports suggest that TiN layers give better confinement of surface plasmon polariton modes [22] compared to gold, though the propagation length is shorter. Also, TiN nanodisks [23] have been shown to heat more efficiently upon illumination than gold disks due to localized surface plasmons. Overall TiN has emerged as a good alternative plasmonic material in the visible spectral range.

$\text{Al}_x\text{Sc}_{1-x}\text{N}$ , on the other hand, behaves as a dielectric material over the entire visible to near-IR spectral range. The  $\epsilon'$  of  $\text{Al}_{0.72}\text{Sc}_{0.28}\text{N}$  has a peak value of 7.2 corresponding to the direct energy gap, after which it decreases slightly and

remains nearly constant at 6.8–7 in the visible to near-UV part of the spectrum (see Fig. 3 in Ref. [15]). The imaginary part of the dielectric permittivity ( $\epsilon''$ ), which is related to the optical loss, decreases as the wavelength moves away from the direct interband transition position. In the region of our interest, i.e.,  $\lambda = 500$  nm and longer, the  $\epsilon''$  is small (in the range of 0.2–0.6) depending on the deposition conditions. For detailed analysis of the optical properties of TiN and (Al,Sc)N, readers are encouraged to refer to Refs. [20] and [15], respectively.

The optical properties of the superlattices have also been evaluated using spectroscopic ellipsometry. Our result for a ten-period 10 nm/10 nm TiN/ $\text{Al}_{0.72}\text{Sc}_{0.28}\text{N}$  superlattice [shown in Fig. 9(a)] suggests that TiN in the superlattice behaves as a plasmonic component for wavelengths longer than 500 nm.  $\epsilon'$  decreases very slowly with increasing wavelength and its magnitude remains under 20 in the entire visible spectral range. However,  $\epsilon''$  for TiN in the visible spectral range is higher compared to noble metals such as gold and silver (about 2), while at longer wavelengths the optical loss is much higher due to free carrier Drude absorption. The

optical properties of  $\text{Al}_{0.72}\text{Sc}_{0.28}\text{N}$  in the superlattice extracted from ellipsometric measurements [Fig. 9(b)] suggest that it behaves as a dielectric in the entire visible to near-IR spectral range as discussed above. The real part of the dielectric permittivity  $\epsilon'$  in the region of our interest (i.e.,  $\sim 500\text{--}2000$  nm spectral range) has a value from 6 to 7 commensurate with that of the magnitude of  $\epsilon'$  of TiN in the same spectral range.

We have employed effective medium theory (EMT) to understand the effective dielectric properties of the superlattices. One has to note that unlike TiN or (Al,Sc)N, the superlattices are anisotropic with strikingly different in-plane ( $\epsilon_{xx} = \epsilon'_{xx} + i\epsilon''_{xx}$ ) and out-of-plane ( $\epsilon_{zz} = \epsilon'_{zz} + i\epsilon''_{zz}$ ) components of the dielectric permittivity. Figure 9(c) suggests that for wavelengths less than 500 nm, where TiN behaves as a dielectric, both  $\epsilon'_{xx}$  and  $\epsilon'_{zz}$  are positive. Positive values of both  $\epsilon'_{xx}$  and  $\epsilon'_{zz}$  lead to the spherical or elliptical dispersion of the isofrequency surfaces for both the  $p$ -polarized and  $s$ -polarized light (normally observed in conventional anisotropic dielectric materials). As seen from Fig. 9(c),  $\epsilon'_{xx}$  is positive, but  $\epsilon'_{zz}$  is negative from 500 to 650 nm. Under such circumstances, the isofrequency surfaces for the  $p$ -polarized light become hyperbolic, and the material is characterized as a type-I or transverse positive HMM. For  $s$ -polarized light however, spherical dispersion is observed. When we increase the wavelength further,  $\epsilon'_{xx}$  becomes negative, while  $\epsilon'_{zz}$  becomes positive. Here, the dispersion relation for the  $p$ -polarized light is hyperbolic, and the material is known as transverse negative or a type-II HMM. Hence, TiN/(Al,Sc)N metal/dielectric superlattices behave as HMMs with both type-I and type-II dispersions in the visible to near-IR spectral ranges. It should be pointed out that none of the traditional HMM systems based on conventional plasmonic materials [6] such as Au and Ag show both type-I and type-II dispersion in the visible to near-IR spectral range.

$\epsilon''$  is related to optical losses and is a critical parameter for practical HMM devices. For wavelengths longer than 500 nm [Fig. 9(d)], when TiN behaves as a dielectric material,  $\epsilon''_{xx}$  and  $\epsilon''_{zz}$  are small. As the wavelength of operation increases into the type-I HMM regime,  $\epsilon''_{zz}$  increases rapidly, while  $\epsilon''_{xx}$

remains small.  $\epsilon''_{zz}$  is maximum at the spectral position when the metamaterial changes hyperbolic dispersion from type I to type II. Above 750 nm, the HMM shows type-II dispersion;  $\epsilon''_{zz}$  decreases while  $\epsilon''_{xx}$  increases due to free carrier absorption.

## B. Transmission and reflection

Transmission ( $T$ ) and reflection ( $R$ ) measurements as a function of the angle of incidence over a broad spectral range provide information about the plasmonic and HMM character of TiN and TiN/(Al,Sc)N superlattices. These measurements also act as a benchmark to validate the ellipsometry-based measurements and data fitting. Figure 10(a) represents the transmittance as a function of the angle of incidence over the visible spectral range for TiN. It suggests that the transmittance ( $T$ ) is maximum in the 440–480 nm spectral range corresponding to the transition from an optical dielectric to metallic characteristics. Transmission also decreases as the angle of incidence is increased as expected for any good plasmonic material. The reflectance ( $R$ ) plotted as a ratio between transverse magnetic (TM) and transverse electric (TE) light [Fig. 10(b)] suggests that TiN is reflecting in virtually the entire visible spectral range except at the spectral position when it changes its character from dielectric to metallic (at 440–480 nm). The reflectance decreases as the angle of incidence is increased. Brewster's angle is apparent between  $\sim 60^\circ$  and  $65^\circ$ , where the reflection from the  $p$ -polarized light vanishes. The reflectance and transmittance measurement does verify our ellipsometric data fitting of TiN.

Transmission and reflection spectra of the superlattice HMMs give deep insight into their properties. The transmittance spectrum from a 10 nm/10 nm ten-period TiN/ $\text{Al}_{0.72}\text{Sc}_{0.28}\text{N}$  superlattice [presented in Fig. 11(a)] suggests that transmission is maximum at 460–500 nm where TiN is slightly metallic. At higher wavelengths, transmission decreases due to large free carrier absorption. The most important aspect of the spectrum is the dip in the transmission in the range of 480–500 nm at higher angles of incidence ( $\sim 60^\circ\text{--}80^\circ$ ) when the metamaterial undergoes the transition from spherical

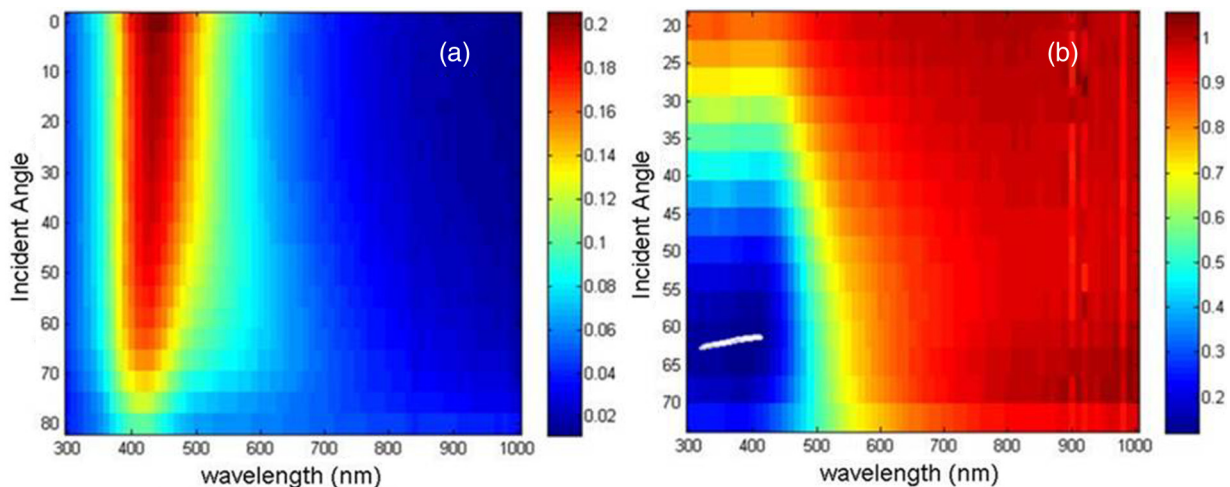


FIG. 10. (Color online) (a) Transmission ( $T$ ) and (b) reflection ( $R$ ) spectra of TiN thin film as a function of the angle of light incidence in the visible spectral range. Brewster's angle is clearly visible in the reflection spectra at  $\sim 60^\circ\text{--}65^\circ$ . Transmission spectra show a peak when TiN becomes plasmonic.

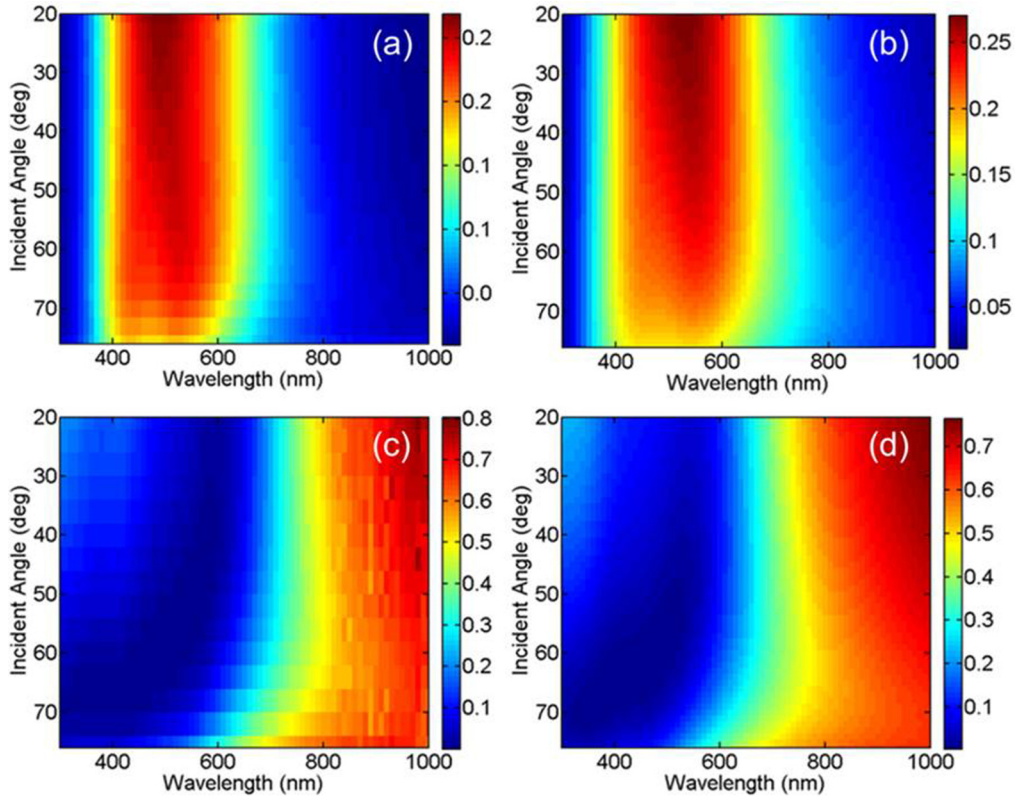


FIG. 11. (Color online) (a) Transmission ( $T$ ) spectra of the  $p$ -polarized light of a 10 nm/10 nm eight-period superlattice plotted as a function of the angle of incidence. A dip in the transmission spectrum is observed owing to the extreme anisotropic nature of the superlattices. (b) The calculated transmission spectrum matches beautifully with the experimental one. (c) Reflection ( $R$ ) spectra of the same superlattice as a function of the angle of incidence. The data is plotted as a ratio between the  $p$ -polarized and the  $s$ -polarized light. Brewster's angle is clearly visible in the spectrum. (d) Calculated reflection spectra of the same superlattice shows excellent agreement between the measurement and theory.

to hyperbolic dispersion of isofrequency surfaces. This dip in transmission is associated with the increasing imaginary component of the wave vector, which is associated with the optical loss as  $\epsilon'_{zz}$  approaches zero. As  $\epsilon'_{zz}$  becomes negative, the optical loss increases, represented by higher values of  $\epsilon''_{zz}$ , and light cannot propagate through the superlattice. However, as the metamaterial changes its dispersion from type I to type II,  $\epsilon''_{zz}$  starts decreasing which means that light can pass through the superlattice and the transmission increases again. The dip in the transmission spectrum represents the anisotropic nature of the superlattice and is strong evidence of the hyperbolic dispersion of the isofrequency surface. The corresponding theoretical calculation of transmittance is presented in Fig. 11(b). The results obtained with the anisotropic transfer matrix approach show excellent agreement with experiment.

The measured reflectance spectrum presented as the ratio between  $p$ -polarized and  $s$ -polarized light [Fig. 11(b)] suggests that for a low angle of incidence, reflectance is very high across the spectral range except for a dip near 600 nm. As the angle of incidence is increased, Brewster's condition is satisfied (i.e., reflection from the  $p$ -polarized light becomes zero) and we see reflectance going to zero. The theoretical calculation [Fig. 11(d)] shows a similar trend and is in good agreement with the measured reflectance. Brewster's angle changes from the high wavelength region of the spectrum to the

low wavelength region (from  $45^\circ$  to  $75^\circ$  in angle of incidence). One should notice that there is no clear evidence of a discontinuity in Brewster's angle. Any discontinuity is obscured by interband transitions and high optical losses in the TiN layers.

### C. Nonlocal field correction

Our description of hyperbolic dispersion in superlattices is subject to the basic assumptions of the EMT. It is known that EMT works well when the individual layer thicknesses in the superlattices are much smaller than the free space wavelength of operation  $\lambda$ , such that the surface plasmon polariton modes at the different metal/dielectric interfaces can couple strongly and effectively with each other [24]. HMM properties of the superlattices are a strong function of this coupling, and EMT can only be used in the strong-coupling regime [25]. Apart from the requirement of the layer thicknesses, EMT also requires field averaging. If the typical field variation length ( $L$ ) is of the order of the wavelength of operation, naturally nonlocal effects will enter into the description of the HMM properties of these superlattices. Elser *et al.* [24] have demonstrated that the conventional EMT fails to describe the properties of metal/dielectric superlattice systems for a majority of nanocomposites. They have also found that EMT only gives satisfactory results when the number of layers in

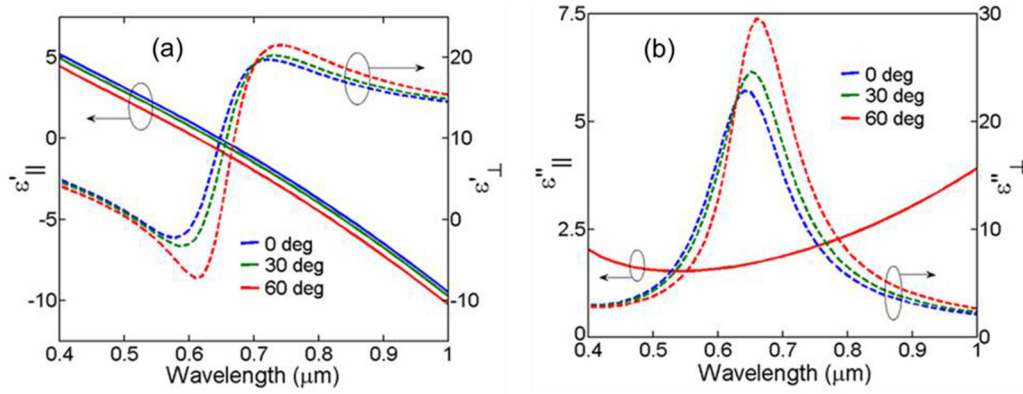


FIG. 12. (Color online) (a) The  $\epsilon'_{xx}$  and  $\epsilon'_{zz}$  of the 10 nm/10 nm eight-period TiN/Al<sub>0.72</sub>Sc<sub>0.28</sub>N superlattice obtained by solving the exact dispersion relation presented in Eqs. (1) and (2) and plotted as a function of the angle of incidence. It is seen that the spectral width of the type-I HMM dispersion increases with an increase in the angle of incidence.

the superlattice is extremely large, even when the individual layer thicknesses are much smaller than the wavelength of light. Therefore, it is important to take into account the nonlocal effects in the description of the HMM properties of the superlattices.

To account for the nonlocal correction in the EMT, we use the exact dispersion of the TM and TE waves in the metal/dielectric systems given by expressions (1) and (2). The wave vectors in the perpendicular ( $\perp$ ) and parallel ( $\parallel$ ) directions are given as

$$\cos(k_{\perp}[a_1 + a_2]) = \cos(k_1 a_1) \cos(k_2 a_2) - \gamma \sin(k_1 a_1) \sin(k_2 a_2), \quad (1)$$

where  $\gamma$  is the polarization specific parameter given by

$$\gamma_{\text{TM}} = \frac{1}{2} \left( \frac{\epsilon_2 k_1}{\epsilon_1 k_2} + \frac{\epsilon_1 k_2}{\epsilon_2 k_1} \right) \quad \text{and} \quad \gamma_{\text{TE}} = \frac{1}{2} \left( \frac{\epsilon_2}{\epsilon_1} + \frac{\epsilon_1}{\epsilon_2} \right),$$

$$k_{1,2} = \frac{\epsilon_{1,2} \omega^2}{c^2} - k_{\parallel}^2, \quad (2)$$

where  $a_1$  and  $a_2$  are the thicknesses of the individual layers.

The in-plane ( $\epsilon_{\parallel}$ ) and the out-of-plane ( $\epsilon_{\perp}$ ) components of the dielectric permittivity calculated using the above expressions are presented in Fig. 12. As we are solving the exact dispersion relation in Eqs. (1) and (2), the solution depends on the angle of incidence of light. As expected, the nonlocal field corrections do not alter the basic nature of the dielectric permittivities, but with increasing angle of incidence, the spectral width of the type-I dispersion of the HMMs increases. The values of  $\epsilon'_{zz}$  also become far more negative as the angle of incidence is increased.

#### D. Role of carrier concentration of TiN

Plasmonic properties and the spectral range of operation of a material depend strongly on its carrier concentration ( $n$ ), carrier mobility ( $\mu$ ), and effective mass ( $m^*$ ) [26]. The number of free electron carriers determines its plasma frequency through the relationship  $\omega_p = 4\pi n e^2 / m^*$ . The conventional plasmonic materials, Au and Ag, have carrier concentrations of  $5.9 \times 10^{22}$  per cc, and  $8 \times 10^{22}$  per cc, respectively, which give rise to their plasmonic properties in the visible to near-UV region of the spectra. However, it is extremely difficult to

change the carrier concentration in elemental noble metals. As a result, one does not have much leverage in tuning the plasma frequency of these metals and altering the operational regime of HMMs consisting of them. On the other hand, TiN can be grown as a thin epitaxial film on different substrates, and the stoichiometry (Ti:N) can also be varied by changing the growth parameters. Changes in stoichiometry of TiN should result in different carrier concentrations, and as a result we should see shifts in the plasma frequency.

We have grown four different TiN/(Al,Sc)N superlattice samples by varying the Ar/N<sub>2</sub> gas ratio during the deposition without changing any other experimental parameters. Ellipsometric characterization and extraction of the individual layer properties suggest that with the increase in the (Ar/N<sub>2</sub>) gas ratio, the carrier concentration of the TiN films decreases from  $3.3 \times 10^{20}$  per cc to  $2.3 \times 10^{20}$  per cc. This modest decrease in the carrier concentration is, however, sufficient to shift  $\lambda_p$  from 490 to 610 nm. The dielectric permittivity of the Al<sub>0.72</sub>Sc<sub>0.28</sub>N layer also changes slightly;  $\epsilon'$  at 1500 nm changes from 5.11 to 6.83 and then back to 4.37, respectively, as the Ar partial pressure is increased during the deposition.

The HMM parameters of the superlattices were evaluated using the effective medium approach. The nature of the dispersion of all the superlattices remains similar to the superlattices discussed in the previous section; however, the spectral position and the bandwidth of type-I HMM dispersion changes considerably with the change in the carrier concentration of the TiN layers. Figure 13 suggests that sample C, which has a TiN carrier concentration of  $3.1 \times 10^{20}$  per cc, has the maximum width of the type-I HMM dispersion (approximately 210 nm, comprising the yellow to red region of the visible spectrum), while the type-I dispersion for sample D extended from 600 to 720 nm. Hence, using different growth parameters, we have been able to tune the plasma frequency of TiN, thus shifting the spectral range and positions of HMM operation.

#### E. Effect of AlN mole fraction in (Al,Sc)N layers and in HMM properties

In this section, we study the effects of the changes in the dielectric permittivity of the (Al,Sc)N layers through variations in the (Al/Sc) ratio, as well as the changes in the

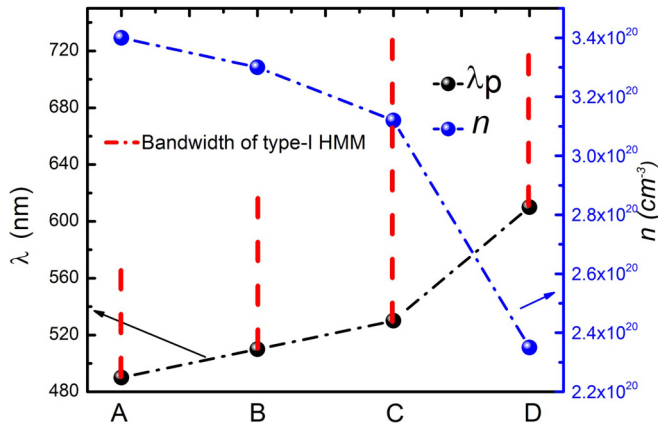


FIG. 13. (Color online) The wavelength ( $\lambda_p$ ) corresponding to the plasma frequency and the carrier concentration ( $n$ ) of four different TiN films in TiN/Al<sub>0.72</sub>Sc<sub>0.28</sub>N superlattices grown at different Ar/N<sub>2</sub> ratio are presented. The spectral width of type-I HMM dispersion is indicated by the vertical lines for each of the four TiN/Al<sub>0.72</sub>Sc<sub>0.28</sub>N superlattice samples termed as A, B, C, and D. It is seen from the figure that sample C, which was grown with a high Ar/N<sub>2</sub> ratio has the highest spectral width for type-I dispersion.

interface roughness on the HMM properties. When the AlN mole fractions in the (Al,Sc)N layers is changed, the lattice parameters also change. Changes in lattice parameter away from the lattice matching condition ( $\sim 68\%$  AlN) increase the lattice mismatch between (Al,Sc)N and TiN, which results in defects originating at the superlattice interfaces in the forms of misfit dislocations and threading dislocations. We have grown three superlattices having ten periods of 10 nm TiN, and 10 nm of Al<sub>0.72</sub>Sc<sub>0.28</sub>N, Al<sub>0.62</sub>Sc<sub>0.38</sub>N, and Al<sub>0.52</sub>Sc<sub>0.48</sub>N layers, respectively. HMM properties are presented in Fig. 14. The ellipsometric fitting of the individual layers suggests that

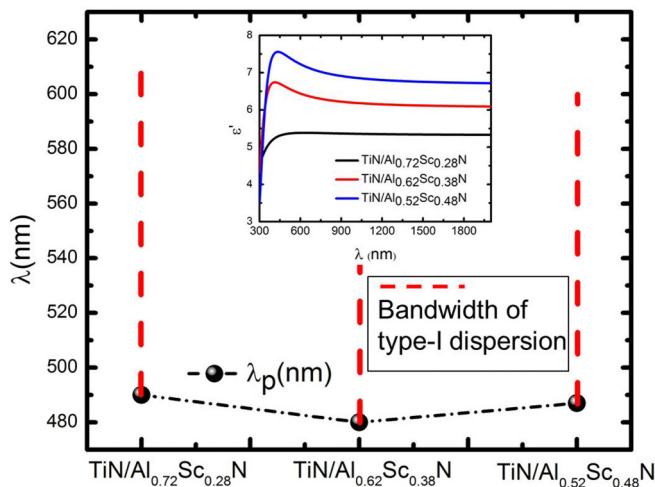


FIG. 14. (Color online) The wavelength ( $\lambda_p$ ) corresponding to the plasma frequency of TiN when the superlattice is grown with a different mole fraction of AlN in Al<sub>x</sub>Sc<sub>1-x</sub>N layers. The vertical lines represent the spectral width of the type-I dispersion curve. The inset in the figure shows a decreasing real part of the dielectric permittivity ( $\epsilon'$ ) of the Al<sub>x</sub>Sc<sub>1-x</sub>N films having as  $x$  increases from 0.52, 0.62 to 0.72.

$\epsilon'$  at 1500 nm changes from 5.11 to 6.12 to 6.75 as the AlN mole fraction is decreased from 0.72 to 0.62 to 0.52. The increase in the permittivity is due to the decrease in the direct band gap of (Al,Sc)N as the AlN mole fraction is reduced (see Ref. [15]). Figure 14 also suggests that  $\lambda_p$  of TiN does not change much (only by 10 nm) with changing AlN mole fraction. Since we are not changing the growth properties of TiN, this small change might be related to the roughening at the interface. The bandwidth of the type-I hyperbolic dispersion also does not change much. Although we see that the losses in the TiN and (Al,Sc)N layers increase slightly with the decrease in  $x$ , the increase in  $\epsilon'$  yields similar widths of the type-I dispersion. Hence we have confirmed that the HMM properties of the superlattice are robust and not very sensitive to small changes in dielectric layer properties and interface roughness.

### F. Effect of substrates

As discussed above, single crystal (001) MgO substrates are the ideal choice for growing TiN/(Al,Sc)N superlattices due to the similarity in the crystal structure of MgO and the transition-metal nitrides. Moreover, there is nearly perfect lattice matching, which assists in growing low-defect-density, high-quality superlattices. However, for practical applications the superlattices have to be deposited on technologically important substrates such as Si and sapphire.

The ellipsometric extraction of the optical properties of the superlattices grown on (0001) sapphire substrates suggests that the TiN layers show plasmonic behavior at 520, 480, and 490 nm, respectively, for 20 nm/20 nm, 10 nm/10 nm, 5 nm/5 nm superlattices [which is consistent with the TiN layers in superlattices grown on (001) MgO substrates]. The  $\epsilon'$  of the Al<sub>0.72</sub>Sc<sub>0.28</sub>N layers, however, changes from 3.27 to 5.28 to 5.90 at the 1000 nm spectral position as the individual layer thickness is decreased from 20 nm to 10 nm to 5 nm. The reason for this sharp change in the values of  $\epsilon'$  is found in the crystal structure of the Al<sub>0.72</sub>Sc<sub>0.28</sub>N layers. We know from our earlier analysis that Al<sub>0.72</sub>Sc<sub>0.28</sub>N layers in its stable form have the wurtzite crystal structure, and we have stabilized them in the rocksalt (cubic) structure using epitaxial stabilization with TiN as the seed layer. Epitaxial stabilization is most effective when the metastable layer thicknesses are small, and there is lattice matching of the metastable layer with the substrate [10, 15]. For 5 and 10 nm Al<sub>0.72</sub>Sc<sub>0.28</sub>N layers grown on top of TiN layers of the same thickness in a superlattice, epitaxial stabilization forces the Al<sub>0.72</sub>Sc<sub>0.28</sub>N layer to be rocksalt (cubic), and as a result,  $\epsilon'$  for these layers is high, similar in comparison with Al<sub>0.72</sub>Sc<sub>0.28</sub>N layers grown on (001) MgO. However, for the 20 nm/20 nm superlattices, epitaxial stabilization is not sufficient to stabilize the 20 nm Al<sub>0.72</sub>Sc<sub>0.28</sub>N layer in the rocksalt (cubic) phase, and the layer takes on its stable wurtzite crystal structure. Wurtzite Al<sub>0.72</sub>Sc<sub>0.28</sub>N has a lower value of  $\epsilon'$  at the same spectral position compared to rocksalt Al<sub>0.72</sub>Sc<sub>0.28</sub>N as the band gap of the wurtzite phase is larger than the band gap of the rocksalt (cubic) phase [15].

Figure 15 also suggests that all of the superlattices undergo a transition from elliptic to type-II hyperbolic dispersion. This is due to the higher optical losses that the individual layers have when grown on (0001) sapphire substrates compared to the case when they are grown on (001) MgO substrates.

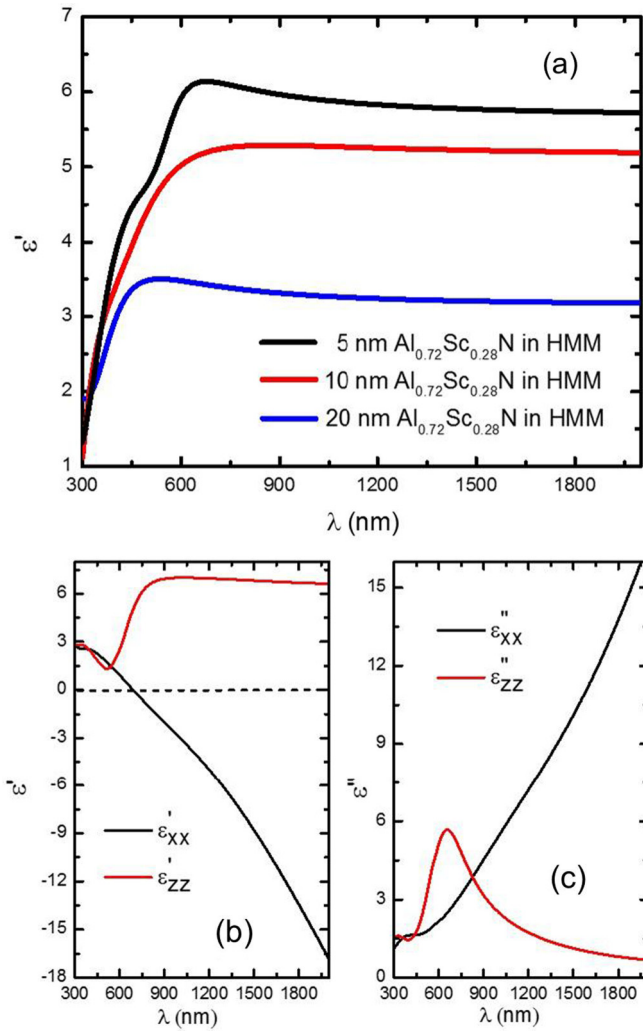


FIG. 15. (Color online) (a) The real part of the dielectric permittivity ( $\epsilon'$ ) of  $\text{Al}_{0.72}\text{Sc}_{0.28}\text{N}$  layers inside  $\text{TiN}/\text{Al}_{0.72}\text{Sc}_{0.28}\text{N}$  superlattices grown on (0001) sapphire substrates. For the 5 nm and 10 nm  $\text{Al}_{0.72}\text{Sc}_{0.28}\text{N}$  layers inside the superlattice the ( $\epsilon'$ ) is high (in the range of 5–6) suggesting that the layers have rocksalt (cubic) structure, but as the layer thickness is increased to 20 nm the  $\epsilon'$  decreases to 3.3 indicating wurtzite structure. (b) The  $\epsilon''_{xx}$  and  $\epsilon''_{zz}$  of the 10 nm/10 nm eight-period  $\text{TiN}/\text{Al}_{0.72}\text{Sc}_{0.28}\text{N}$  superlattice. It is seen from the figure that the HMM has only type-II dispersion. There is no type-I dispersion as  $\epsilon''_{zz}$  never becomes negative. (c)  $\epsilon''_{xx}$  and  $\epsilon''_{zz}$  of the HMM that has a very high value owing to the greater optical loss of the individual layers.

Figure 15 also indicates that for the 20 nm/20 nm superlattice,  $\epsilon''_{zz}$  decreases beyond 430 nm up to 520 nm, but does not become negative to give type-I dispersion as the  $\epsilon'$  of the  $\text{Al}_{0.72}\text{Sc}_{0.28}\text{N}$  layer is too small and the optical losses of the individual layers are very high. For the 10 nm/10 nm, and 5 nm/5 nm superlattices, although  $\epsilon''_{zz}$  is very small in the 500–600 nm spectral range, it is still positive due to higher losses, and no type-I dispersion is achieved here as well.  $\epsilon''_{xx}$ , however, is negative at 700, 730, and 830 nm for the 20 nm/20 nm, 10 nm/10 nm, and 5 nm/5 nm superlattices, respectively, which creates the type-II hyperbolic dispersion for this spectral range.

The optical properties of the superlattices grown on (001) Si substrates resemble those grown on (0001) sapphire substrates. Type-I hyperbolic dispersion in the superlattices grown on Si substrates has not been observed, for the same reasons noted above for superlattices on sapphire. The important point to notice is that the  $\text{Al}_{0.72}\text{Sc}_{0.28}\text{N}$  layers are not stable in the (rocksalt) cubic phase even when the layer thickness is 10 nm. This reduces the  $\epsilon'$  values of the  $\text{Al}_{0.72}\text{Sc}_{0.28}\text{N}$  layers and results in positive  $\epsilon''_{zz}$  over the 600–200 nm spectral range. Similar to the superlattices grown on (0001) sapphire substrates, the  $\epsilon''_{xx}$  does become negative in these cases also, giving rise to type-II dispersion from the red part of the visible spectrum to the near-IR spectral range.

Though the  $\text{TiN}/(\text{Al,Sc})\text{N}$  superlattices grown on Si (001) substrates are polycrystalline, we must emphasize that it is possible to grow epitaxial superlattices on Si substrates with an appropriate choice of a buffer layer. Shinkai *et al.* [27] have demonstrated the growth of single-orientation HfN on (001) and (111) Si substrates. Therefore, using HfN as a buffer layer we should be able to deposit epitaxial superlattices on Si substrates.

### G. Comparative studies and CMOS compatibility of $\text{TiN}/(\text{Al,Sc})\text{N}$ HMMs

The performance of an HMM can be determined by its so called figure-of-merit (FOM) defined [6,14] as  $\text{Re}(\beta_{\perp})/\text{Im}(\beta_{\perp})$  where  $\beta_{\perp}$  is the propagation constant of light in the direction perpendicular to the layers. Figure of merit also serves as a metric for comparing optical performance of different HMMs in various regions of the spectra. We have presented the FOM of the  $\text{TiN}/(\text{Al,Sc})\text{N}$  superlattices grown on MgO substrates and compare its performance with that of traditional noble-metal-based HMMs such as  $\text{Ag}/\text{SiO}_2$  and  $\text{Au}/\text{Al}_2\text{O}_3$  with a 50% metal fill fraction on each case [14] (see Fig. 16). Figure 16 suggests that the  $\text{TiN}/(\text{Al,Sc})\text{N}$  HMMs outperform

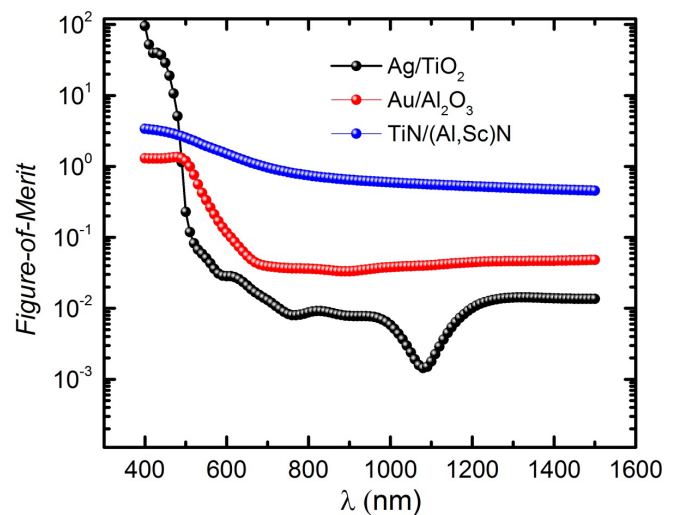


FIG. 16. (Color online) FOM [6] [ $\text{Re}(\beta_{\perp})/\text{Im}(\beta_{\perp})$ ] of  $\text{TiN}/(\text{Al,Sc})\text{N}$  superlattices grown on MgO substrates. The FOM of  $\text{Ag}/\text{TiO}_2$  and  $\text{Au}/\text{Al}_2\text{O}_3$  are also presented, which suggests that the  $\text{TiN}$ -based HMMs outperform the conventional noble-metal-based HMMs in the visible to near-IR spectral range.

their Ag- and Au-based counterparts in the entire visible to near-IR spectral range. The maximum FOM achieved with TiN/(Al,Sc)N superlattices is about 3 at 500 nm when TiN becomes metallic, while the FOM for the noble-metal-based counterpart is less than 1.

The nitride superlattices HMMs developed here are technologically important because of their compatibility with silicon-CMOS technology. TiN is already used as a barrier layer in the dual damascene process [28]. However, it must be mentioned that though TiN can be integrated easily with CMOS technology, the dc-magnetron sputtering process with which we have deposited our thin films and superlattices at high growth temperature (750 °C–850 °C) is not CMOS compatible. Therefore, it is necessary to use low temperature (<500 °C) growth processes, which can in principle be addressed by using alternative deposition techniques such as chemical vapor deposition (CVD) and atomic layer deposition (ALD). These methods have been optimized to produce good electrical quality TiN films at low temperatures [29] (i.e., CMOS compatible).

AlScN is not used in CMOS processes. However, it does not pose any major incompatibility with CMOS devices or processes. Similar to TiN, a low-temperature deposition of AlScN is possible if ALD or CVD is employed as a deposition technique instead of magnetron sputtering.

#### IV. CONCLUSION

In conclusion, we have developed monocrystalline, pseudomorphic, epitaxial TiN/(Al,Sc)N metal/dielectric superlattices as a novel class of optical hyperbolic metamaterials that do not require traditional plasmonic components such as silver and gold. These superlattices show both type-I and type-II hyperbolic dispersion of its isofrequency surfaces, which cannot be simultaneously obtained in other HMM systems. X-ray diffraction studies reveal that the superlattices grown on (001) MgO substrate are pseudomorphic, coherent, and grow with (002) orientation having a small degree of mosaicity. X-ray reflectivity studies suggest that the superlattice interfaces are atomically sharp with an interface roughness on the order

of one to two atomic layers. High-resolution TEM along with the MAADF-STEM confirms high-quality sharp and abrupt interfaces and excellent crystal properties. Superlattices grown on (0001) sapphire substrates were shown to grow with (111) orientations with multiple variants, while the superlattices grown on (001) Si substrates were found to be polycrystalline. The optical properties of the superlattices have been studied by spectroscopic ellipsometry. It has been demonstrated that TiN behaves as a plasmonic component in the green part of the visible spectrum at ~480–500 nm spectral range. Both transverse negative (or type-I) and transverse positive (or type-II) hyperbolic dispersion of  $p$ -polarized light has been achieved in the visible to near-IR spectral range. Angle-dependent transmission measurements showed a dip in transmission at ~500 nm spectral range, which suggests that the superlattices are highly anisotropic. We have used the effective medium approximation to describe the HMM properties of the superlattices. The nonlocal effects, which are not captured in the standard EMT, have also been incorporated in our description through solving the nonlinear exact dispersion relation. It has been shown that the basic behavior of the dispersion does not change, while the spectral width of the observed type-I dispersion does vary. We have also discussed the effects of the changing carrier concentration in TiN and the mole fraction ( $x$ ) of AlN in the  $\text{Al}_x\text{Sc}_{1-x}\text{N}$  layer on the HMM properties. Finally, we have discussed the superlattice HMM properties grown directly on (0001) sapphire and (001) Si substrates. The TiN/(Al,Sc)N metal/dielectric superlattices developed here represent a new generation of epitaxial thin-film-based plasmonic and HMM systems with enhanced optical properties.

#### ACKNOWLEDGMENTS

B.S. and T.D.S. acknowledge financial support by the National Science Foundation and the U.S. Department of Energy (CBET-1048616). E.A.S acknowledges support to the Center for Functional Nanomaterials, Brookhaven National Laboratory, which is supported by the U.S. Department of Energy, Office of Basic Energy Sciences, under Contract No. DE-AC02-98CH10886.

- 
- [1] A. Poddubny, I. Iorsh, P. Belov, and Y. Kivshar, *Nat. Photonics* **7**, 948 (2013).
  - [2] C. L. Cortes, W. Newman, S. Molesky, and Z. Jacob, *J. Opt.* **14**, 063001 (2012).
  - [3] Z. Liu, H. Lee, Y. Xiong, C. Sun, and X. Zhang, *Science* **315**, 1685 (2007).
  - [4] Z. Jacob, L. V. Alekseyev, and E. Narimanov, *Optics Express* **14**, 8247 (2006).
  - [5] J. A. Schuller, E. S. Barnard, W. Cai, Y. C. Jun, J. S. White, and M. L. Brongersma, *Nat. Mater.* **9**, 193 (2010).
  - [6] A. J. Hoffman, L. Alekseyev, S. S. Howard, K. J. Franz, D. Wasserman, V. A. Podolskiy, E. E. Narimanov, D. L. Sivco, and C. Gmachl, *Nat. Mater.* **6**, 946 (2007).
  - [7] G. V. Naik, J. Liu, A. V. Kildishev, V. M. Shalaev, and A. Boltasseva, *Proc. Natl. Acad. Sci. USA* **109**, 8834 (2012).
  - [8] H. N. Krishnamoorthy, Z. Jacob, E. Narimanov, I. Kretzschmar, and V. M. Menon, *Science* **336**, 205 (2012).
  - [9] J. Kim, V. P. Drachev, Z. Jacob, G. V. Naik, A. Boltasseva, E. E. Narimanov, and V. M. Shalaev, *Opt. Express* **20**, 8100 (2012).
  - [10] G. V. Naik, B. Saha, J. Liu, S. M. Saber, E. A. Stach, J. M. K. Irudayaraj, T. D. Sands, V. M. Shalaev, and A. Boltasseva, *Proc. Natl. Acad. Sci.* **111**, 7546 (2014)..
  - [11] Y. Guo and Z. Jacob, *Opt. Express* **21**, 15014 (2013).
  - [12] U. Guler, A. Boltasseva, and V. M. Shalaev, *Science* **344**, 263 (2014).

- [13] S. A. Maier, M. L. Brongersma, P. G. Kik, S. Meltzer, A. A. G. Requicha, and H. A. Atwater, *Adv. Mater.* **13**, 1501 (2001).
- [14] G. V. Naik, V. M. Shalaev, and A. Boltasseva, *Adv. Mater.* **25**, 3264 (2013).
- [15] B. Saha, S. Saber, G. V. Naik, A. Boltasseva, E. Stach, E. Kvam, and T. D. Sands, *Physica Status Solidi. B: Basic Research* (to be published).
- [16] E. Chason and T. M. Mayer, *Crit. Rev. Solid State Mater. Sci.* **22**, 1 (1997).
- [17] E. Chason, C. M. Falco, A. Ourmazd, E. F. Schubert, J. M. Slaughter, and R. S. Williams, *Mater. Res. Soc. Symp. Proc.* **280**, 203 (1993).
- [18] C. Sun, S. Lee, W. Hwang, J. Hwang, I. Tang, and Y. S. Fu, *Mater. Trans.* **47**, 2533 (2006).
- [19] D. Williams and C. B. Carter, *Transmission Electron Microscopy* (Springer, New York, 1996), pp. 376–380; The upper collection angle is limited in this environmental microscope to 70 mrad. Therefore, it is not fully in Z-contrast mode. Nevertheless, the contrast is correlated with the average atomic number.
- [20] G. V. Naik, J. L. Schroeder, X. Ni, A. V. Kildishev, T. D. Sands, and A. Boltasseva, *Opt. Mater. Express* **2**, 478 (2012).
- [21] B. Saha, J. Acharya, T. D. Sands, and U. V. Waghmare, *J. Appl. Phys.* **107**, 033715 (2010).
- [22] N. Kinsey, M. Ferrera, G. V. Naik, V. E. Babicheva, V. M. Shalaev, and A. Boltasseva, *Opt. Express* **22**, 12238 (2014).
- [23] U. Gular, J. C. Ndukaife, G. V. Naik, A. G. A. Nnanna, A. V. Kildishev, V. M. Shalaev, and A. Boltasseva, *Nano Lett.* **13**, 6078 (2013).
- [24] J. Elser, V. A. Podolskiy, I. Salakhutdinov, and I. Avrutsky, *Appl. Phys. Lett.* **90**, 191109 (2007).
- [25] A. V. Chebykin, A. A. Orlov, C. R. Simovski, Yu. S. Kivshar, and P. A. Belov, *Phys. Rev. B* **86**, 115420 (2012).
- [26] A. Boltasseva and H. A. Atwater, *Science* **331**, 290 (2011).
- [27] S. Shinkai and K. Sasaki, *Jpn. J. Appl. Phys.* **38**, 2097 (1999).
- [28] J. C. Lin, R. Augur, S. L. Shue, C. H. Yu, M. S. Liang, A. Vijayendran, T. Suwwan de Felipe, and M. Danek, in *Proceedings of the IEEE 2002 International Interconnect Technology Conference, Hyatt Regency Hotel, Burlingame, CA* (IEEE, Piscataway, NJ, 2002), pp. 21–23.
- [29] S. Kurtz and R. Hordon, *Thin Solid Films* **140**, 277 (1986); S. Heil, E. Langereis, F. Roozeboom, M. Sanden, and W. Kessels, *J. Electrochem. Soc.* **153**, G956 (2006).